Effect of Pt vacancies on magnetotransport of Weyl semimetal candidate GdPtSb epitaxial films

Dongxue Du,[1] Laxman Raju Thoutam [iD],[2,3] Konrad T. Genser,[4] Chenyu Zhang,[1] Karin M. Rabe,[4] Tamalika Samanta,[1] Taehwan Jung,[1] Bharat Jalan,[3] Paul M. Voyles [iD],[1] and Jason K. Kawasaki [iD][1,*]

[1]*Materials Science and Engineering, University of Wisconsin-Madison, Madison, Wisconsin 53706, USA*
[2]*Amrita School of Nanosciences and Molecular Medicine, Amrita Vishwa Vidyapeetham, Ponekkara, Kochi 682041, India*
[3]*Department of Chemical Engineering and Materials Science, University of Minnesota—Twin Cities, Minneapolis, Minnesota 55455, USA*
[4]*Department of Physics and Astronomy, Rutgers University, New Brunswick, New Jersey 08901, USA*

We examine the effects of Pt vacancies on the magnetotransport properties of Weyl semimetal candidate GdPtSb films, grown by molecular beam epitaxy on c-plane sapphire. Rutherford backscattering spectrometry and x-ray diffraction measurements suggest that phase-pure $GdPt_xSb$ films can accommodate up to 15% of Pt vacancies ($x = 0.85$), which act as acceptors, as measured by the Hall effect. Two classes of electrical transport behavior are observed. Pt-deficient films display metallic temperature-dependent resistivity ($d\rho/dT > 0$). The longitudinal magnetoresistance (LMR, magnetic field **B** parallel to electric field **E**) is more negative than transverse magnetoresistance (TMR, **B** $\perp$ **E**), consistent with the expected chiral anomaly for a Weyl semimetal. The combination of Pt-vacancy disorder and doping away from the expected Weyl nodes, however, suggests that conductivity fluctuations may explain the negative LMR rather than chiral anomaly. Samples closer to stoichiometry display the opposite behavior: semiconductorlike resistivity ($d\rho/dT > 0$) and more negative TMR than LMR. Hysteresis and other nonlinearities in the low-field Hall effect and magnetoresistance suggest that spin-disorder scattering and possible topological Hall effect may dominate the near-stoichiometric samples. Our findings highlight the complications of transport-based identification of Weyl nodes but point to possible topological spin textures in GdPtSb.

I. INTRODUCTION

The lanthanide half-Heusler compounds LnPtBi and LnPtSb are attractive due to their tunable topological and magnetic properties as functions of lanthanide substitution [1–3], strain [2], and strain gradients [4]. Compounds in this family of materials were among the first identified as zero band gap topological semimetals via density functional theory (DFT) [2], with confirmation for LuPtSb [5], LuPtBi [6], and YPtBi [6] by angle-resolved photoemission spectroscopy measurements [5,6].

More recently, band structure calculations and magnetotransport measurements have suggested that GdPtBi [7,8], TbPtBi [9], HoPtBi [9], and ErPtBi [9] compounds are magnetic-field-induced Weyl semimetals. In these materials, Zeeman or exchange splitting is expected to lift the degeneracy of quadratic bands that touch at Γ to create pairs of Weyl nodes [7,8]. One experimental signature of these Weyl nodes is the chiral anomaly: charge pumping between Weyl nodes of opposite chirality when an applied magnetic field **B** is parallel to the electric field **E** [10,11]. This appears as a negative longitudinal magnetoresistance (LMR) with a characteristic angle dependence **E** · **B** and has been observed in several LnPtBi compounds [7–9,11].

A fundamental challenge, however, is that negative LMR is not unique to the chiral anomaly. Other mechanisms for negative LMR include current jetting [11,12], conductivity fluctuations [12–14], suppression of surface scattering [15], and spin-disorder scattering above magnetic transition temperatures in magnetically ordered materials [16]. Thus, it is difficult to identify a chiral anomaly via negative LMR alone [17]. In half-Heusler compounds, conductivity fluctuations may contribute because these materials are highly susceptible to natural nonstoichiometry [18] and variations in atomic site ordering [19], due to the low formation energies for point defects. Moreover, since LnPtBi and LnPtSb are typically antiferromagnetic below $T_N \sim 10$ K, spin-disorder scattering is likely to play a role.

Here, we explore the magnetotransport properties of GdPtSb, which like GdPtBi is seen in band structure calculations to have quadratic bands that touch at Γ. We explore the effects of naturally occurring Pt vacancies on magnetotransport of GdPtSb films grown by molecular beam epitaxy on c-plane sapphire substrates. We find that the angle-dependent magnetoresistance depends strongly on Pt stoichiometry and comment on the relative roles of chiral anomaly, conductivity fluctuations, spin-disorder scattering, and topological Hall effect in $GdPt_xSb$. Our observation of hysteresis plateaus in the low-field Hall resistivity in near-stoichiometric GdPtSb suggests a topological Hall effect which may arise from topological spin textures.

II. METHODS

A. Molecular beam epitaxy

We synthesize GdPtSb films by molecular beam epitaxy on (0001)-oriented Al_2O_3 substrates, using conditions like in

*jkawasaki@wisc.edu

Ref. [20]. The growth temperature is 600 °C. The Gd flux was supplied by a thermal effusion cell. A Sb_2/Sb_1 mixture was supplied by a thermal cracker cell with a cracker zone operated at 1200 °C. The Pt flux was supplied by an electron beam evaporator. Fluxes were measured *in situ* using a quartz crystal microbalance immediately prior to growth. Absolute compositions were measured by Rutherford backscattering spectrometry (RBS). Due to the high relative volatility of Sb, GdPtSb films were grown in an Sb adsorption-controlled regime with a 30% excess Sb flux, such that the Sb stoichiometry is self-regulated [21].

B. First-principles calculations

Calculations were done with ABINIT using the PBE-GGA exchange correlation potential and norm-conserving pseudopotentials from ONCVPSP-3.3.0, except for the Gd pseudopotential, which was constructed to have the f orbitals in the core. The k-point mesh used was $18 \times 18 \times 18$, and the energy cutoff was 1400 eV (50 Hartree). Computed lattice parameters for the half-Heusler structure were 6.647 Å for GdPtSb and 6.777 Å for GdPtBi in the conventional face-centered cubic unit cell.

C. Transport measurements and Hall effect fitting

Magnetotransport measurements for $GdPt_xSb$ samples were performed using a Quantum Design Dynacool Physical Property Measurement System. Hall effect measurements were generally performed in a Hall bar geometry with typical dimensions of 5×1 mm. For the $x = 0.85$ sample, the Hall effect was measured in a van der Pauw geometry. To correct for contact misalignments that mix ρ_{xx} and ρ_{xy}, we note that, for magnetic materials, the transverse resistivity must obey the relation $\rho_{xy,R}(B) = -\rho_{xy,L}(-B)$, where the subscript R denotes increasing magnetic field and L denotes a decreasing field direction. Thus, the symmetrized transverse resistivities are

$$\rho_{xy,R,\text{symm}}(B) = \frac{\rho_{xy,R}(B) - \rho_{xy,L}(-B)}{2},$$

$$\rho_{xy,L,\text{symm}}(B) = \frac{\rho_{xy,L}(B) - \rho_{xy,R}(-B)}{2}.$$

Angle-dependent magnetoresistance measurements were performed using a horizontal rotator probe and contacts in a squeeze test geometry. The center channel is a standard linear four-point geometry with contacts in a line down the center of the sample, where the outer contacts are current and the inner contacts are voltage. The edge channel uses the same current contacts but places the voltage contacts at the edge of the sample to test the effects of current jetting down the center of the sample.

To extract carrier densities, we fit the Hall data to a two-band model of the following form:

$$\rho_{xy}^{\text{normal}}(B) = \frac{B}{e} \frac{\left(n_h \mu_h^2 - n_e \mu_e^2\right) + (n_h - n_e)\mu_h^2 \mu_e^2 B^2}{(n_h \mu_h + n_e \mu_e)^2 + (n_h - n_e)^2 \mu_h^2 \mu_e^2 B^2},$$

where n_h (n_e) and μ_h (μ_e) are concentration and mobility of holes (electrons). We constrain the two-band Hall fit by also
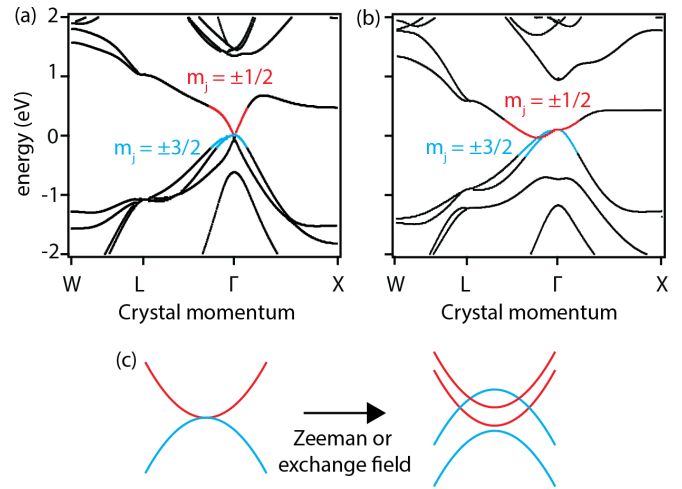

FIG. 1. Density functional theory (DFT) calculations. (a) DFT-GGA band structures of GdPtSb and (b) GdPtBi. The bands near the Fermi energy at Γ have strong Sb $5p_{3/2}$ or Bi $6p_{3/2}$ character. Red denotes the $m_j = \pm\frac{1}{2}$ states, and blue denotes the $m_j = \pm\frac{3}{2}$ states. (c) Cartoon showing how the quadratic band touching at Γ splits due to exchange or Zeeman splitting to form pairs of Weyl nodes with opposite chiralities.

fitting to the zero magnetic field longitudinal resistivity:

$$\rho_{xx}(0) = \frac{1}{e(n_h \mu_h + n_e \mu_e)}.$$

We use the carrier concentration to estimate the Fermi level positions. For a rough estimation, we used three-dimensional parabolic band density of states:

$$D(E) = \frac{\sqrt{2}}{\pi^2} \frac{(m^*)^{3/2}}{\hbar^3} \sqrt{E},$$

where m^* is the effective mass:

$$m^* = \frac{\hbar^2}{d^2 E / dk^2}.$$

We calculated the effective mass for the three valence bands near $E = 0$ eV at the Γ point, based on our band structure calculation in Fig. 1. The Fermi level is extracted from the following integral:

$$\sum_{n=1}^{2 \text{ or } 3} \int_0^{E_F} D(E)\, dE = \frac{N}{V}.$$

From the above calculation, the E_F for the $x = 0.84$ sample with hole concentration 2.72×10^{20} cm^{-3} is about -170 meV, and that for the $x = 0.96$ sample with hole concentration 1.75×10^{19} cm^{-3} is about -40 meV.

D. Magnetization measurements

Magnetic properties were measured using a Quantum Design MPMS superconducting quantum interference device (SQUID) magnetometer. The magnetic field is applied perpendicular to the sample surface. The net magnetization data for the $GdPt_xSb$ thin films are extracted by subtracting a background measurement of the Al_2O_3 substrate from the total magnetization signal.

E. Transmission electron microscopy

Here, GdPtSb cross-section samples were prepared with a Zeiss Ga-focused ion beam, followed by final thinning in a Fishione Model 1040 Nanomill using Ar ions at 900 V. Samples were stored in vacuum and cleaned in a GV10× DS Asher cleaner at 20 W for 10 min to remove contamination and minimize the oxidization on the sample before being transferred into the scanning transmission electron microscopy (STEM) column. A probe-corrected Thermo-Fisher Titan STEM equipped with CEOS aberration corrector operated at 200 kV was used to collect the atomic-resolution STEM images. A 24.5 mrad probe semiangle, 18.9 pA probe current was used to collect high-angle annular dark-field (HAADF) image series with a Fishione 3000 annular detector covering collection angle ranging from 53.9 to 269.5 mrad. Each frame in the image series took ∼0.6 s to acquire with 10 μs on each STEM scan position and 256×256 scan grid. Nonrigid registration [22] was used to compensate for the drift and distortions during image series acquisition, before the series was averaged to get a single frame with high signal-to-noise ratio, as shown in Fig. 2(d).

F. X-ray diffraction

X-ray diffraction (XRD) measurements were performed using a Malvern Empyrean diffractometer with Cu $K\alpha$ radiation.

G. RBS

RBS measurements were performed at the University of Minnesota Characterization Facility.

III. RESULTS

We first establish the possibility of Weyl nodes for GdPtSb using DFT calculations. In the well-studied material GdPtBi, the essential feature is a quadratic band touching of four Bi $6p$ $j = \frac{3}{2}$ states near the Fermi energy [Fig. 1(b)]. The Zeeman or exchange energy splits the $m_j = \pm\frac{3}{2}$ and $m_j = \pm\frac{1}{2}$ to create Weyl nodes near the Fermi energy [Fig. 1(c)] [7,8].

Our nonmagnetic DFT calculations suggest that GdPtSb replicates this essential feature, with a quadratic touching of Sb $5p$ $j = \frac{3}{2}$ states at the Fermi energy at Γ [Fig. 1(a)]. However, we note that, for GdPtSb, there is an additional hole band ∼60 meV below the charge neutrality point (0 eV) at Γ that may complicate the transport by providing an additional conduction channel. For GdPtBi, this hole band is pushed further down to ∼700 meV, presumably due to the larger spin-orbit coupling for Bi than Sb.

XRD and reflection high-energy electron diffraction (RHEED) measurements reveal that epitaxial (111)-oriented GdPt$_x$Sb films with half-Heusler structure are readily stabilized under Pt-deficient conditions [Fig. 2(a)]. For $x = 0.85$–1, only the anticipated 111-type reflections are observed by XRD, indicating phase-pure half-Heusler growth. The corresponding streaky RHEED patterns indicate smooth epitaxial films. Samples closer to stoichiometry show an enhanced intensity of the higher-order 333 and 444 XRD reflections
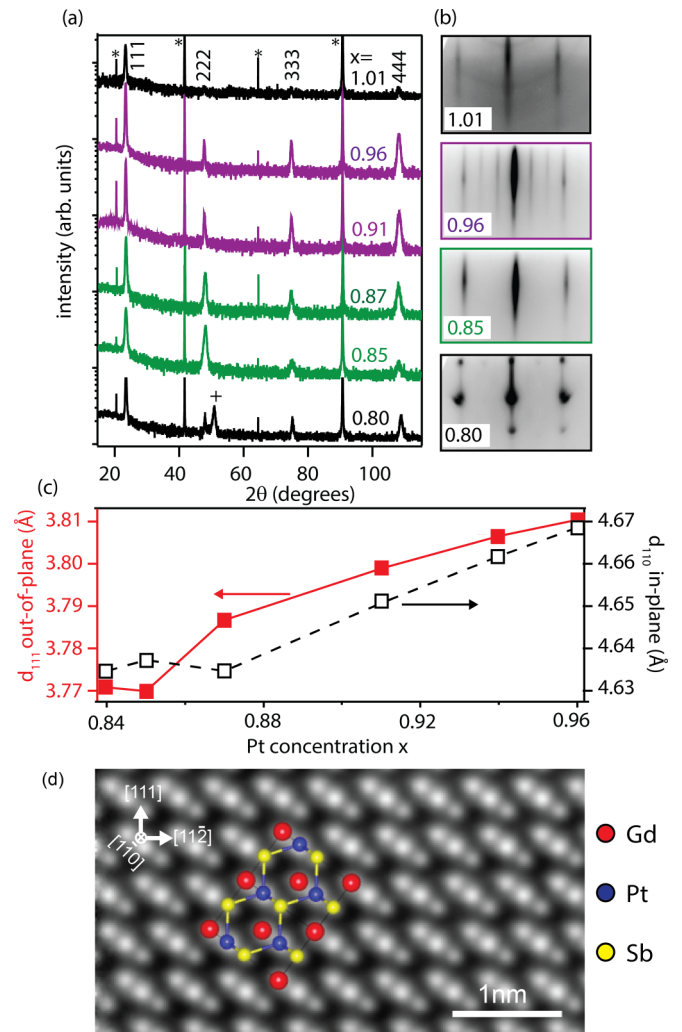

FIG. 2. Structures and basic transport properties of stoichiometric and Pt-deficient GdPtSb epitaxial films. (a) X-ray diffraction [Cu $K\alpha$ of (111)-oriented GdPt$_x$Sb thin films grown on Al$_2$O$_3$ (0001)]. The * indicates Al$_2$O$_3$ substrate reflections. The + sign for $x = 0.80$ denotes a GdSb impurity phase. (b) Corresponding reflection high-energy electron diffraction (RHEED) patterns. (c) Out-of-plane (d_{111}, red) and in-plane (d_{110}, blue) lattice spacings extracted from on-axis 222 and off-axis 202 reflections. (d) High-angle annular dark-field (HAADF) scanning transmission electron microscopy (STEM) image of GdPtSb, measured along a $\langle 110 \rangle$ zone axis. Red denotes columns of Gd atoms, blue is Pt, and yellow is Sb.

and a well-ordered 3× surface reconstruction by RHEED compared with the 1× periodicity for Pt-deficient films ($x = 0.85$). For highly Pt-deficient conditions, $x \leqslant 0.8$, we observe precipitation of a secondary GdSb phase by XRD and rough three-dimensional growth by RHEED [Fig. 2(b)]. For Pt-rich conditions, $x > 1.01$, the higher-order 222, 333, and 444 half-Heusler XRD reflections disappear, and we observe faint polycrystalline rings in the RHEED pattern [Fig. 2(b)].

Focusing on the phase-pure GdPt$_x$Sb samples with $x = 0.85$–1, we observe a systematic increase for the out-of-plane d_{111} and in-plane d_{110} lattice spacings [Fig. 2(c)]. The in-plane d_{110} spacings are calculated from measurements of an off-axis 202 reflection [see Supplemental Material [23], Fig. S1]. The
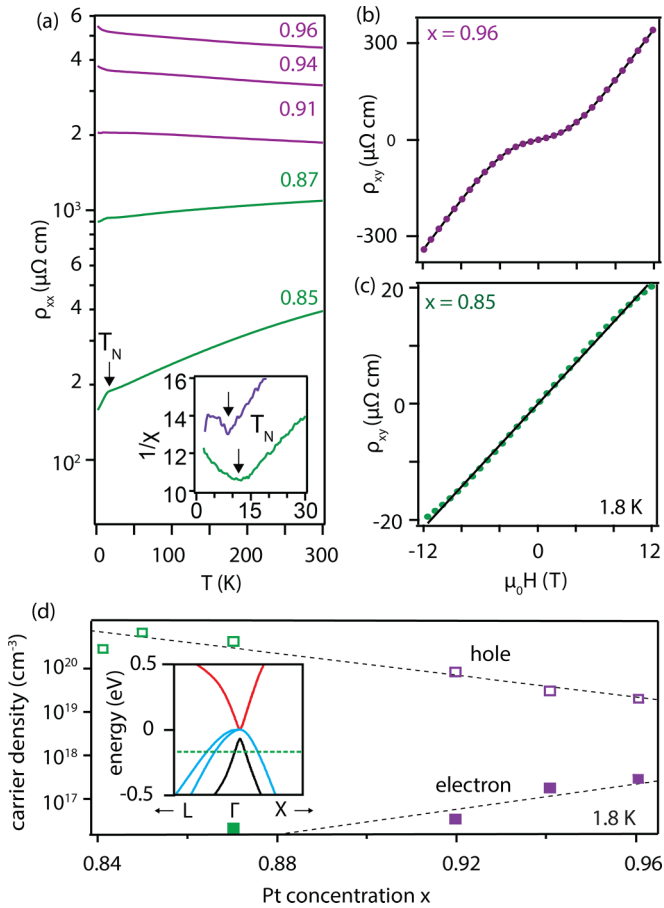
FIG. 3. (a) Zero-field resistivity for GdPt$_x$Sb with different Pt concentrations. Inset shows the inverse magnetic susceptibility vs temperature for the $x = 0.85$ (green) and $x = 0.96$ (purple) samples measured by superconducting quantum interference device (SQUID), showing the Néel transition. (b) Transverse (Hall) resistivity for the $x = 0.96$ sample, measured at 1.8 K. The black line is an ordinary Hall effect two-band model fit. (c) Hall effect at 1.8 K for the $x = 0.85$ sample showing near linear behavior. (d) Hall carrier density vs Pt concentration at 1.8 K, extracted from fitting to a model with one electron and one hole. The inset shows the approximate position of the Fermi energy for $x = 0.85$ in a two-band model with one electron and one hole.

observed Pt-deficient samples are consistent with DFT calculations that predict Pt vacancies are the lowest-energy defects for the related compound LuPtSb [25]. HAADF-STEM measurements of the $x = 0.85$ sample shown in Fig. 2(d) are in agreement with the expected site ordering for GdPtSb in cubic half-Heusler structure (space group $F\bar{4}3m$). Here, the brightest atomic columns correspond to columns of Pt atoms (which have the largest atomic mass), followed by columns of Gd and columns of Sb.

Zero-field resistivity measurements of near-stoichiometric GdPtSb films ($x > 0.9$) display an insulatorlike temperature dependence [$d\rho/dT < 0$, Fig. 3(a), purple]. We attribute the insulatorlike resistivity to the Fermi energy being near the quadratic band touching (Fig. 1). In contrast, for heavily Pt-deficient samples ($x < 0.9$), we observe metallic transport [$d\rho/dT > 0$, Fig. 3(a), green]. We attribute the more metallic transport to doping induced by Pt vacancies.

SQUID magnetometry measurements reveal a sharp antiferromagnetic Néel transition at $T_N \approx 9$ K for the $x = 0.96$ sample, as determined from a minimum in the inverse susceptibility $1/\chi$ vs temperature [Fig. 3(a), insert]. For samples with $x < 0.9$, the transition in $\chi(T)$ is broader, however, we observe a peak in $d\rho/dT$ at 9 K, which likely corresponds to the Neel transition (Supplemental Material [23], Fig. S2).

Hall effect measurements reveal that Pt vacancies in GdPtSb are acceptors. The heavily Pt-deficient samples ($x < 0.9$) show a positive and near linear dependence of the Hall resistivity ρ_{xy} on the magnetic field [Fig. 3(c)], indicating dominant hole carriers. Closer to stoichiometry ($x > 0.9$), the samples show stronger nonlinearities that are well fit by a two-band model with one hole and one electron for $\mu_0|H| > 1$ T [Fig. 3(b)]. Figure 3(d) summarizes the effective electron and hole densities vs Pt concentration x, extracted from fitting to the two-band model (Methods). Note that, in reality, there are 2–3 hole bands near the Fermi energy; however, since we cannot distinguish these bands from a simple Hall effect fitting, we emphasize that these are *effective* carrier densities. We find that charge neutrality $n = p$ appears as x approaches 1, and the effect of Pt vacancies is to increase the hole density and decrease the electron density. Based on a three-dimensional parabolic band model (Methods), we estimate that the Fermi energy for the $x = 0.85$ sample, which has effective hole density $p = 2.72 \times 10^{20}$ cm^{-3}, lies 170 meV below the charge neutrality point. For the $x = 0.96$ sample ($p = 1.75 \times 10^{19}$ cm^{-3}, $n = 2.5 \times 10^{17}$ cm^{-3}), we estimate the Fermi energy is $\sim$40 meV below the charge neutrality point. We caution that, while we call this $x = 0.96$ sample *near stoichiometric*, the hole density is still nearly two orders of magnitude larger than the electron density ($p \gg n$).

Intriguingly, the near-stoichiometric GdPtSb sample with $x = 0.96$ displays low field hysteresis in $\rho_{xy}(H)$ that is highly suggestive of the topological Hall effect, which is often a signature of chiral spin textures such as skyrmions [26,27]. Figure 4(a) replots $\rho_{xy}(H)$ at 2 K focusing on the low-field region $\mu_0|H| < 2$ T. We observe two hysteresis loops centered at -0.5 and 0.5 T (respectively, red and blue curves) that deviate strongly from the normal Hall effect. In general, the transverse Hall signal can be decomposed into normal, anomalous, and topological components, $\rho_{xy}^{\text{total}} = \rho_{xy}^{\text{normal}} + \rho_{xy}^{\text{anom}} + \rho_{xy}^{\text{topo}}$. The normal component results from the Lorentz force on free carriers. At high field ($\mu_0|H| > 1$T), the sample is well fit to a two-band model [Fig. 3(b)], whereas at low field ($\mu_0|H| < 1$T), the hysteresis deviates strongly from the two-band model [Fig. 3(a), dotted black line]. The anomalous component is proportional to the magnetization, $\rho_{xy}^{\text{anom}} \propto M$. Our preliminary SQUID measurements show linear $M(H)$ for field up to 0.4 T [Fig. 4(c)], which is within the range of observed hysteresis for ρ_{xy}. This suggests that the hysteresis does not arise from the anomalous component and that the topological Hall effect is a likely origin; however, we caution that further magnetization measurements beyond 1 T are needed to fully analyze the data. To understand the possible topological origin, in Fig. 4(b), we plot $\rho_{xy}^{\text{total}} - \rho_{xy}^{\text{normal}}$, which equals the sum of the anomalous Hall effect and the topological Hall effect. A similar topological
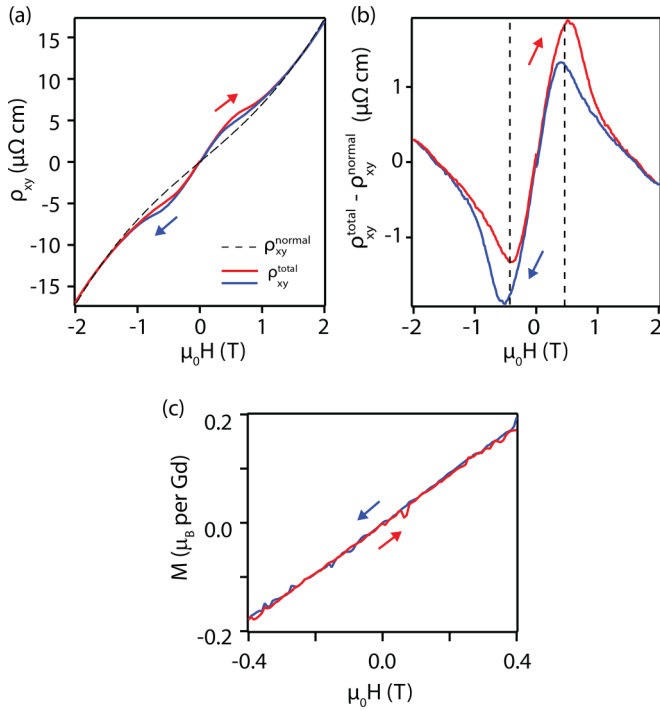
FIG. 4. Topological Hall effect. (a) Hall resistivity vs field for the $x = 0.96$ sample, measured at 2 K. The red and blue lines are measured Hall resistivity ρ_{xy}^{total} with increasing (red) and decreasing (blue) magnetic field. The black dashed line shows normal Hall fit $\rho_{xy}^{\text{normal}}$. (b) Total Hall resistance subtracted by normal Hall fit ρ_{xy}^{total}-$\rho_{xy}^{\text{normal}}$. The plotted signal is a sum of the anomalous Hall effect and the topological Hall effect $\rho_{xy}^{\text{anom}} + \rho_{xy}^{\text{topo}}$. The dashed lines mark the $\mu_0 H = \pm 0.4$ T positions. (c) Out-of-plane magnetization vs field, measured at 1.8 K by superconducting quantum interference device (SQUID).

Hall effect has also been suggested for GdPtBi [28] but has not yet been confirmed by real-space measurements of spin textures.

We now analyze the magnetoresistance as a function of the angle θ between **B** and **E**. The chiral anomaly, i.e., charge pumping between Weyl nodes, is expected to produce an additional current that is proportional to **B** · **E**. Therefore, for Weyl semimetals, the magnetoresistance $\Delta\rho/\rho_0$ should be negative for $\theta = 0$ and become more positive with increasing θ [7,29–31]. Figure 5(a) shows the angle-dependent magnetoresistance of the Pt-deficient $x = 0.85$ sample, measured at 1.8 K using voltage contacts along the edge of the sample and current sourced along the center of the sample [Fig. 5(c)]. We find that the LMR ($\theta = 0°$) is negative and the transverse magnetoresistance (TMR, $\theta = 90°$) is positive, as expected for the chiral anomaly. A continuously varying angular dependence, in a van der Pauw geometry, is shown in Fig. S3 [23]. The general angular dependence is qualitatively like previous studies of GdPtBi single crystals [7,11]. However, the magnitude of change for our epitaxial GdPtSb films is only a few percent, whereas the magnetoresistance change for GdPtBi crystals is ∼80%.

The $x = 0.85$ sample passes the squeeze test [11], suggesting that current jetting is not the primary origin

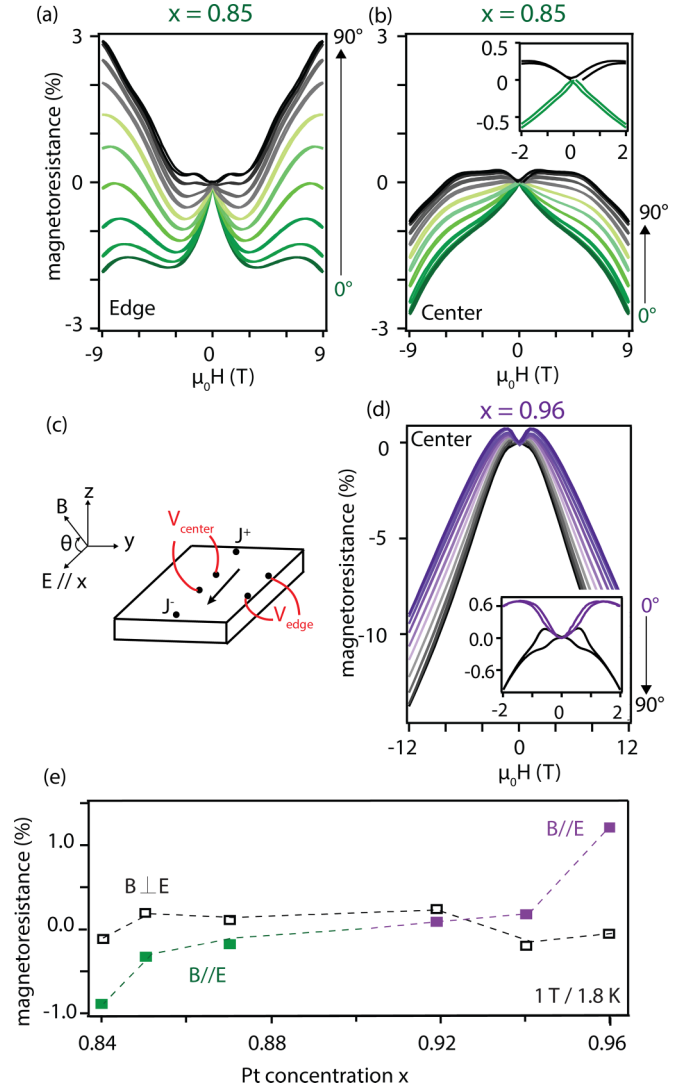FIG. 5. Chiral anomaly tests. (a) and (b) Magnetoresistance for a Pt-deficient $x = 0.85$ sample, as a function of angle θ between **B** and **E**, in steps of $\Delta\theta = 10°$, where $\theta = 90°$ corresponds to the out-of-plane field. Comparison of voltage contacts (a) along the edge with those (b) along the center constitutes the squeeze test for analyzing the contribution of extrinsic current jetting. (c) Measurement geometry, where **B** ≈ μ_0**H** since $M \ll H$. (d) Angle-dependent magnetoresistance for a near-stoichiometric $x = 0.96$ sample, in steps of $\Delta\theta = 10°$. Inset shows hysteresis for $\theta = 90°$. (e) Longitudinal (**B** ∥ **E**) and transverse (**B** ⊥ **E**) magnetoresistance at 1 T and 1.8 K for samples with varying Pt concentration.

of the negative LMR. Here, we find that measurements with contacts along the center of the sample [Fig. 5(b)] produce the same qualitative behavior as edge contacts [Fig. 5(a)], namely, negative LMR and positive TMR at modest magnetic field ($\mu_0|H| < 6$ T). Two-point resistance measurements also produce the negative magnetoresistance for $\theta = 0$ that increases with θ (see Supplemental Material [23], Fig. S4), confirming that current jetting is not a dominant factor. Furthermore, current jetting effects are expected to be strongest for materials with high carrier mobility and anisotropic conduction [11]. Our samples have more modest

Hall effect mobility ($\mu \sim 50$ cm^2/Vs) and are expected to be isotropic in the (111) plane compared with reports of single crystals that have higher mobility of 1500 cm^2/Vs at 6 K [7].

Near-stoichiometric samples display the opposite angular dependence. Figure 5(d) shows the angle-dependent magnetoresistance for a sample with composition $x = 0.96$, measured at 1.8 K. In addition to a weak positive magnetoresistance at low field ($\mu_0|H| < 4$ T) and low θ, the magnetoresistance is generally negative and becomes more negative with increasing θ. This is opposite the expected dependence for chiral anomaly, which is expected to produce the most negative magnetoresistance for $\theta = 0$. Additionally, the TMR shows a weak hysteresis within the range $\mu_0|H| < 1$ T [Fig. 5(d), insert], the same range as observed for the Hall resistance [Fig. 4(a)]. Minimal hysteresis is observed in the magnetoresistance of the $x = 0.85$ sample.

We summarize the TMR and LMR at field 1 T and temperature 1.8 K for several samples with varying Pt concentration in Fig. 5(e). For Pt-deficient samples ($x < 0.9$), the LMR (**B** ∥ **E**) is generally more negative than the TMR (**B** ⊥ **E**), as expected for chiral anomaly. For samples closer to stoichiometry ($x > 0.9$), the LMR is generally more positive than TMR. This dependence on Pt concentration is opposite the expectation for chiral anomaly, which we expect to be strongest for stoichiometric samples in which the Fermi energy is closer to the Weyl nodes ($x \approx 1$). Previous experiments on doped GdPtBi show that the negative LMR is maximized near the charge neutrality point [7].

IV. DISCUSSION

What explains the Pt stoichiometry dependence? For Pt-deficient samples ($x < 0.9$), the Pt-vacancy disorder and position of the Fermi energy away from the Weyl nodes suggest that conductivity fluctuations rather than chiral anomaly may dominate. For inhomogeneous or disordered materials, spatial fluctuations in the conductivity can lead to a component of the carrier velocity that is perpendicular to **B**, even when the global **E** is parallel to **B** [12–14,32,33]. The resulting Lorentz force leads to a decrease in the LMR with increasing **B**. We expect Pt-deficient samples to show these fluctuations more strongly than stoichiometric samples. Moreover, the very Pt-deficient samples have Fermi energy furthest away from the expected Weyl nodes and thus are not anticipated to show strong effects from chiral anomaly compared with samples closer to stoichiometry ($x \approx 1$).

For samples closer to stoichiometry, trivial bands near the Fermi energy and spin-disorder scattering may explain the negative LMR. We first note that, unlike the well-studied Weyl semimetal GdPtBi, GdPtSb has an additional hole band ~ 60 meV below the charge neutrality point [Fig. 1(a)] that may contribute to the transport and obscure the chiral anomaly.

Additionally, in magnetically ordered materials like GdPtSb (which is antiferromagnetic), field alignment of spins or other forms of spin-disorder scattering can also cause a negative LMR [16,34,35], and the angular dependence can arise from magnetocrystalline anisotropy or shape anisotropy. For reasons that are still unclear, the effects of magnetic ordering are more prominent for our near-stoichiometric GdPtSb
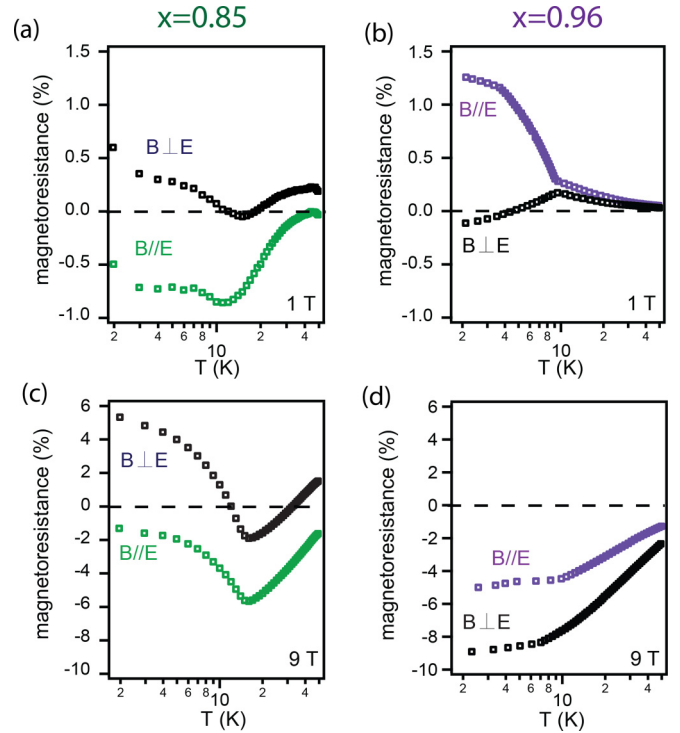

FIG. 6. Temperature dependence of the longitudinal magnetoresistance (LMR) and transverse magnetoresistance (TMR). (a) $x = 0.85$ sample at 1 T. (b) $x = 0.95$ sample at 1 T. (c) $x = 0.85$ sample at 1 9 T. (e) $x = 0.95$ sample at 9 T. These measurements were performed in a van der Pauw geometry. Note the magnitudes are different than in Fig. 5 due to the different contact geometry.

samples than for heavily Pt-deficient samples. First, the TMR of the $x = 0.96$ sample shows magnetic hysteresis that does not appear for the $x = 0.85$ sample [Figs. 5(b) and 5(d), insets]. Second, the temperature-dependent magnetoresistance for the $x = 0.96$ sample at low field diverges below $T_N \sim 9$ K [Fig. 6(b)], where the LMR increases and the TMR decreases with decreasing temperature. In contrast, the LMR and TMR for the $x = 0.85$ sample do not diverge below T_N [Fig. 6(a)]. Further magnetization studies, as a function of magnetic field orientation, are required to understand the mechanisms for the angle-dependent magnetoresistance in near-stoichiometric samples.

V. CONCLUSIONS

We demonstrate that half-Heusler GdPt$_x$Sb epitaxial films grown on sapphire accommodate a large concentration of Pt vacancies, which act as acceptors. Samples with high Pt-vacancy concentration have a metallic resistivity vs temperature and display a negative LMR that becomes more positive as the magnetic field tilts away from the electric field, consistent with a chiral anomaly. However, the large concentration of Pt vacancies and position of the Fermi energy away from the Weyl nodes suggest that conductivity fluctuations, rather than chiral anomaly, dominates. Samples closer to stoichiometry show an insulatorlike resistivity vs temperature and TMR that is more negative than LMR, opposite the expected

behavior of chiral anomaly. The low-field Hall effect shows nonlinearities like the topological Hall effect. Further detailed magnetotransport, magnetometry, and real-space imaging are required to understand the possible balance of Weyl nodes and topological spin textures in GdPtSb.

ACKNOWLEDGMENTS

[1] Y. Nakajima, R. Hu, K. Kirshenbaum, A. Hughes, P. Syers, X. Wang, K. Wang, R. Wang, S. R. Saha, D. Pratt *et al.*, Sci. Adv. **1**, e1500242 (2015).

[2] H. Lin, L. A. Wray, Y. Xia, S. Xu, S. Jia, R. J. Cava, A. Bansil, and M. Z. Hasan, Nat. Mater. **9**, 546 (2010).

[3] K. Gofryk, D. Kaczorowski, T. Plackowski, A. Leithe-Jasper, and Y. Grin, Phys. Rev. B **84**, 035208 (2011).

[4] D. Du, S. Manzo, C. Zhang, V. Saraswat, K. T. Genser, K. M. Rabe, P. M. Voyles, M. S. Arnold, and J. K. Kawasaki, Nat. Commun. **12**, 2494 (2021).

[5] J. A. Logan, S. Patel, S. D. Harrington, C. Polley, B. D. Schultz, T. Balasubramanian, A. Janotti, A. Mikkelsen, and C. J. Palmstrøm, Nat. Commun. **7**, 11993 (2016).

[6] Z. Liu, L. Yang, S.-C. Wu, C. Shekhar, J. Jiang, H. Yang, Y. Zhang, S.-K. Mo, Z. Hussain, B. Yan *et al.*, Nat. Commun. **7**, 12924 (2016).

[7] M. Hirschberger, S. Kushwaha, Z. Wang, Q. Gibson, S. Liang, C. A. Belvin, B. A. Bernevig, R. J. Cava, and N. P. Ong, Nat. Mater. **15**, 1161 (2016).

[8] C. Shekhar, N. Kumar, V. Grinenko, S. Singh, R. Sarkar, H. Luetkens, S.-C. Wu, Y. Zhang, A. C. Komarek, E. Kampert *et al.*, Proc. Natl. Acad. Sci. U.S.A. **115**, 9140 (2018).

[9] J. Chen, H. Li, B. Ding, E. Liu, Y. Yao, G. Wu, and W. Wang, Appl. Phys. Lett. **116**, 222403 (2020).

[10] S. L. Adler, Phys. Rev. **177**, 2426 (1969).

[11] S. Liang, J. Lin, S. Kushwaha, J. Xing, N. Ni, R. J. Cava, and N. P. Ong, Phys. Rev. X **8**, 031002 (2018).

[12] R. Dos Reis, M. Ajeesh, N. Kumar, F. Arnold, C. Shekhar, M. Naumann, M. Schmidt, M. Nicklas, and E. Hassinger, New J. Phys. **18**, 085006 (2016).

[13] J. Hu, T. F. Rosenbaum, and J. B. Betts, Phys. Rev. Lett. **95**, 186603 (2005).

[14] T. Schumann, M. Goyal, D. A. Kealhofer, and S. Stemmer, Phys. Rev. B **95**, 241113(R) (2017).

[15] M. Steele, Phys. Rev. **97**, 1720 (1955).

[16] K. Usami, J. Phys. Soc. Jpn. **45**, 466 (1978).

[17] X.-T. Xu and S. Jia, Chin. Phys. B **25**, 117204 (2016).

[18] Y. G. Yu, X. Zhang, and A. Zunger, Phys. Rev. B **95**, 085201 (2017).

[19] S. Öğüt and K. M. Rabe, Phys. Rev. B **51**, 10443 (1995).

[20] D. Du, A. Lim, C. Zhang, P. J. Strohbeen, E. H. Shourov, F. Rodolakis, J. L. McChesney, P. Voyles, D. C. Fredrickson, and J. K. Kawasaki, APL Mater. **7**, 121107 (2019).

[21] E. H. Shourov, R. Jacobs, W. A. Behn, Z. J. Krebs, C. Zhang, P. J. Strohbeen, D. Du, P. M. Voyles, V. W. Brar, D. D. Morgan *et al.*, Phys. Rev. Mater. **4**, 073401 (2020).

[22] A. B. Yankovich, B. Berkels, W. Dahmen, P. Binev, S. I. Sanchez, S. A. Bradley, A. Li, I. Szlufarska, and P. M. Voyles, Nat. Commun. **5**, 4155 (2014).

[23] See Supplemental Material at http://link.aps.org/supplemental/10.1103/PhysRevMaterials.7.084204 for extraction of lattice parameters, determination of Neel transition from transport, magnetoresistance versus angle, and two point resistivity test, which includes Ref. [24].

[24] M. E. Fisher and J. Langer, Phys. Rev. Lett. **20**, 665 (1968).

[25] S. Khalid, H. S. Inbar, S. Chatterjee, C. J. Palmstrom, and A. Janotti, arXiv:2208.05415.

[26] A. Neubauer, C. Pfleiderer, B. Binz, A. Rosch, R. Ritz, P. G. Niklowitz, and P. Böni, Phys. Rev. Lett. **102**, 186602 (2009).

[27] V. Kumar, N. Kumar, M. Reehuis, J. Gayles, A. S. Sukhanov, A. Hoser, F. Damay, C. Shekhar, P. Adler, and C. Felser, Phys. Rev. B **101**, 014424 (2020).

[28] T. Suzuki, R. Chisnell, A. Devarakonda, Y.-T. Liu, W. Feng, D. Xiao, J. W. Lynn, and J. Checkelsky, Nat. Phys. **12**, 1119 (2016).

[29] J. Xiong, S. K. Kushwaha, T. Liang, J. W. Krizan, M. Hirschberger, W. Wang, R. J. Cava, and N. P. Ong, Science **350**, 413 (2015).

[30] S. A. Parameswaran, T. Grover, D. A. Abanin, D. A. Pesin, and A. Vishwanath, Phys. Rev. X **4**, 031035 (2014).

[31] H. B. Nielsen and M. Ninomiya, Phys. Lett. B **130**, 389 (1983).

[32] J. Hu, M. M. Parish, and T. F. Rosenbaum, Phys. Rev. B **75**, 214203 (2007).

[33] J. Xu, M. K. Ma, M. Sultanov, Z.-L. Xiao, Y.-L. Wang, D. Jin, Y.-Y. Lyu, W. Zhang, L. N. Pfeiffer, K. W. West *et al.*, Nat. Commun. **10**, 287 (2019).

[34] L. Ritchie, G. Xiao, Y. Ji, T. Y. Chen, C. L. Chien, M. Zhang, J. Chen, Z. Liu, G. Wu, and X. X. Zhang, Phys. Rev. B **68**, 104430 (2003).

[35] C. N. Borca, T. Komesu, H.-K. Jeong, P. A. Dowben, D. Ristoiu, C. Hordequin, J. P. Nozieres, J. Pierre, S. Stadler, and Y. U. Idzerda, Phys. Rev. B **64**, 052409 (2001).